nature climate change

SUPPLEMENTARY INFORMATION

DOI: 10.1038/NCLIMATE2055

Mid-latitude westerlies as a driver of glacier variability in monsoonal

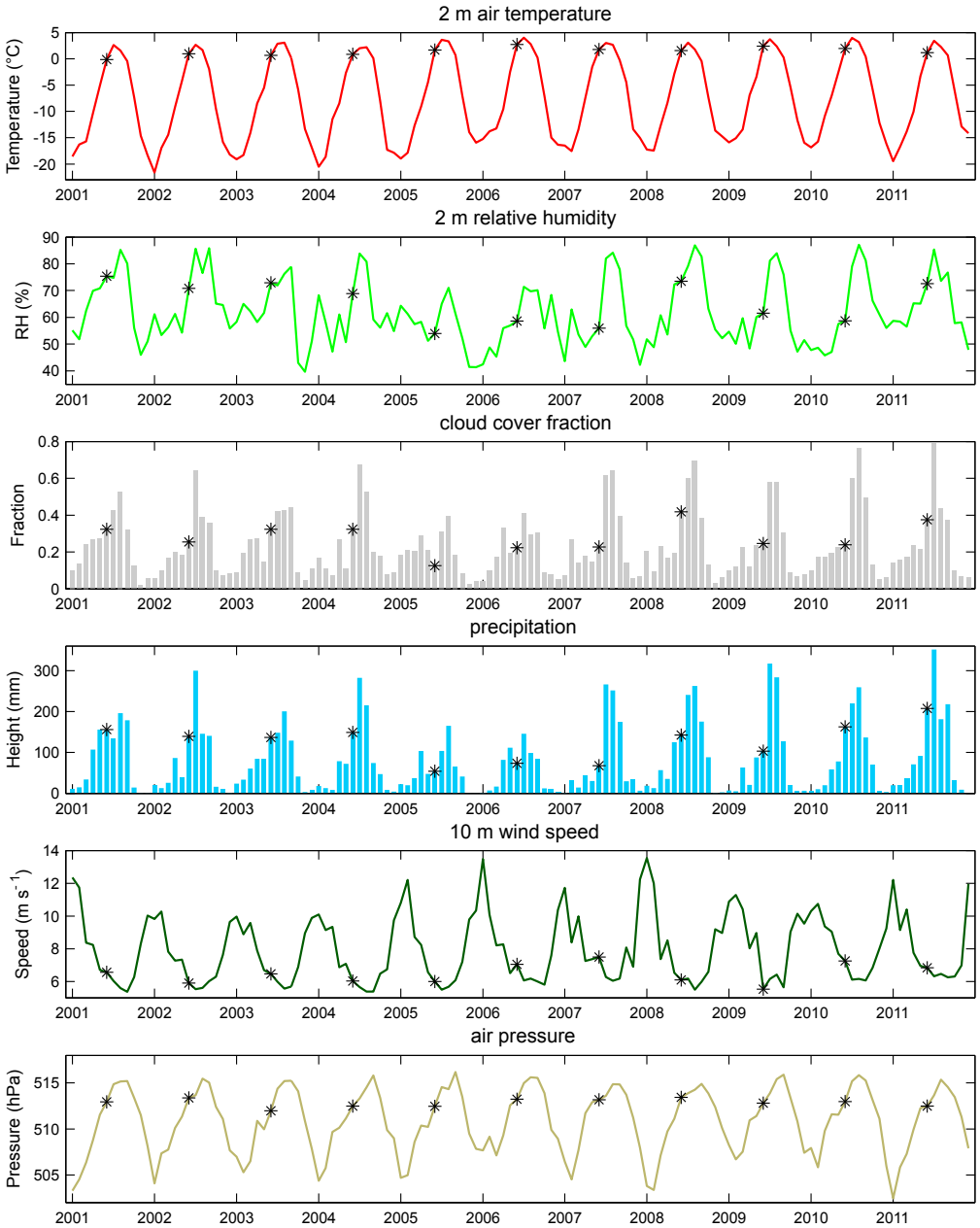

Figure S1: Monthly means or sums (precipitation) of meteorological variables at the atmospheric model grid cell containing Zhadang Glacier (domain 2, 5611 m), 2001-2011. Ticks on the x-axes indicate January of the respective year, and asterisks the month June (which coincides closely with the ISM onset period). Note that the MB model is forced with hourly values of these six variables, so monthly values here do not show the full range of the MB forcing but rather a climatic overview.

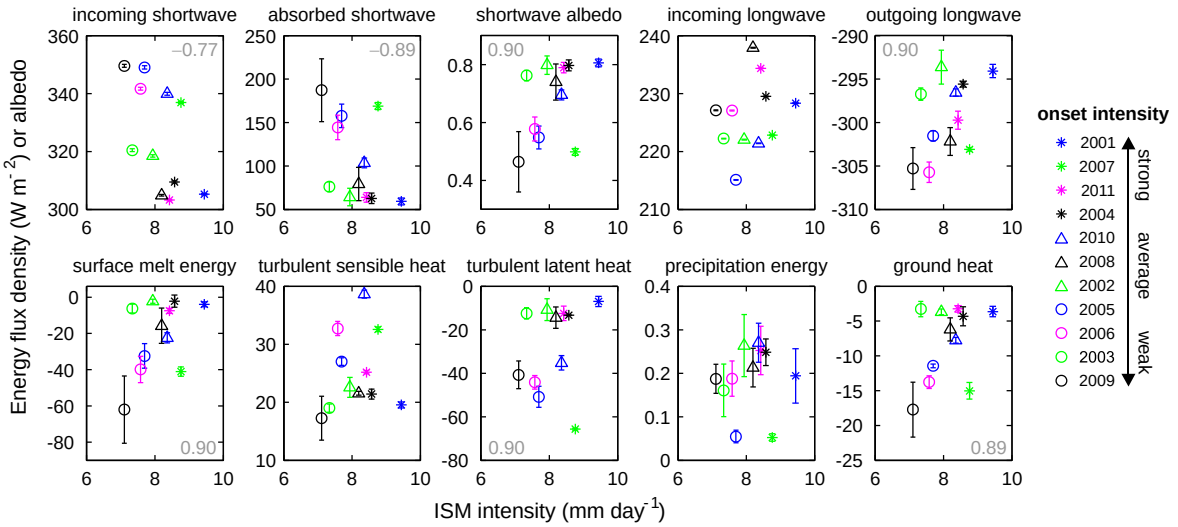

Figure S2: Precipitation in the ISM region versus glacier-wide energy balance components during the ISM onset period. Broadband albedo is also shown. The legend identifies the years and provides the order of the ISM onset intensity. As in Fig. 3 of the main paper, statistically significant correlations ($p < 0.05$) are given for all years in black (i.e., no case here) and without 2002/2003/2007 (grey). Note the different scaling of the y-axes, and the largest y-axis range of absorbed shortwave radiation (which controls the surface melt energy response). Surface energy sinks (gains) are negative (positive). Error bars as defined in Supplementary Methods.

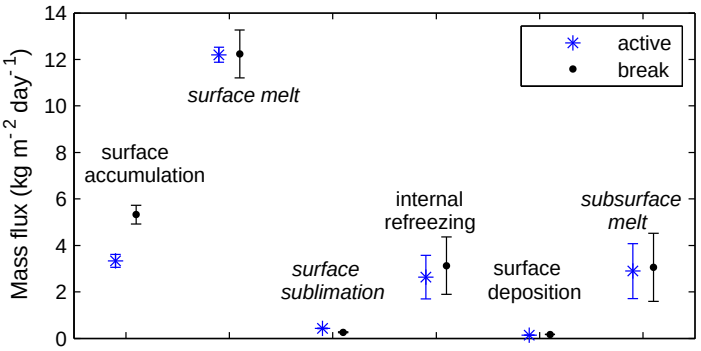

Figure S3: Glacier-wide MB components averaged over active and break days (see Supplementary Methods) of the ISM main seasons 2001-2011. Normal (italics) font signifies mass gain (mass loss) terms, error bars as defined in Supplementary Methods.

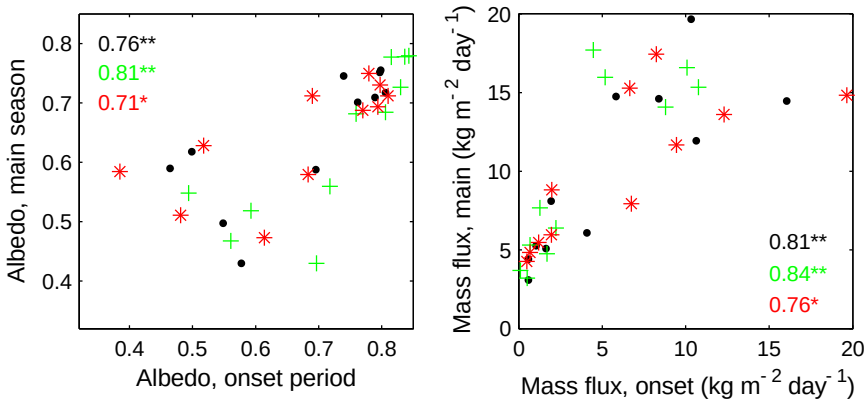

Figure S4: Glacier-wide (left) albedo and (right) surface melt flux in the main ISM season as a function of the ISM onset period, 2001-2011, in the three model runs (different colours/symbols; see Supplementary Methods). Correlation coefficients and significance level (** 0.01, * 0.05) are given.

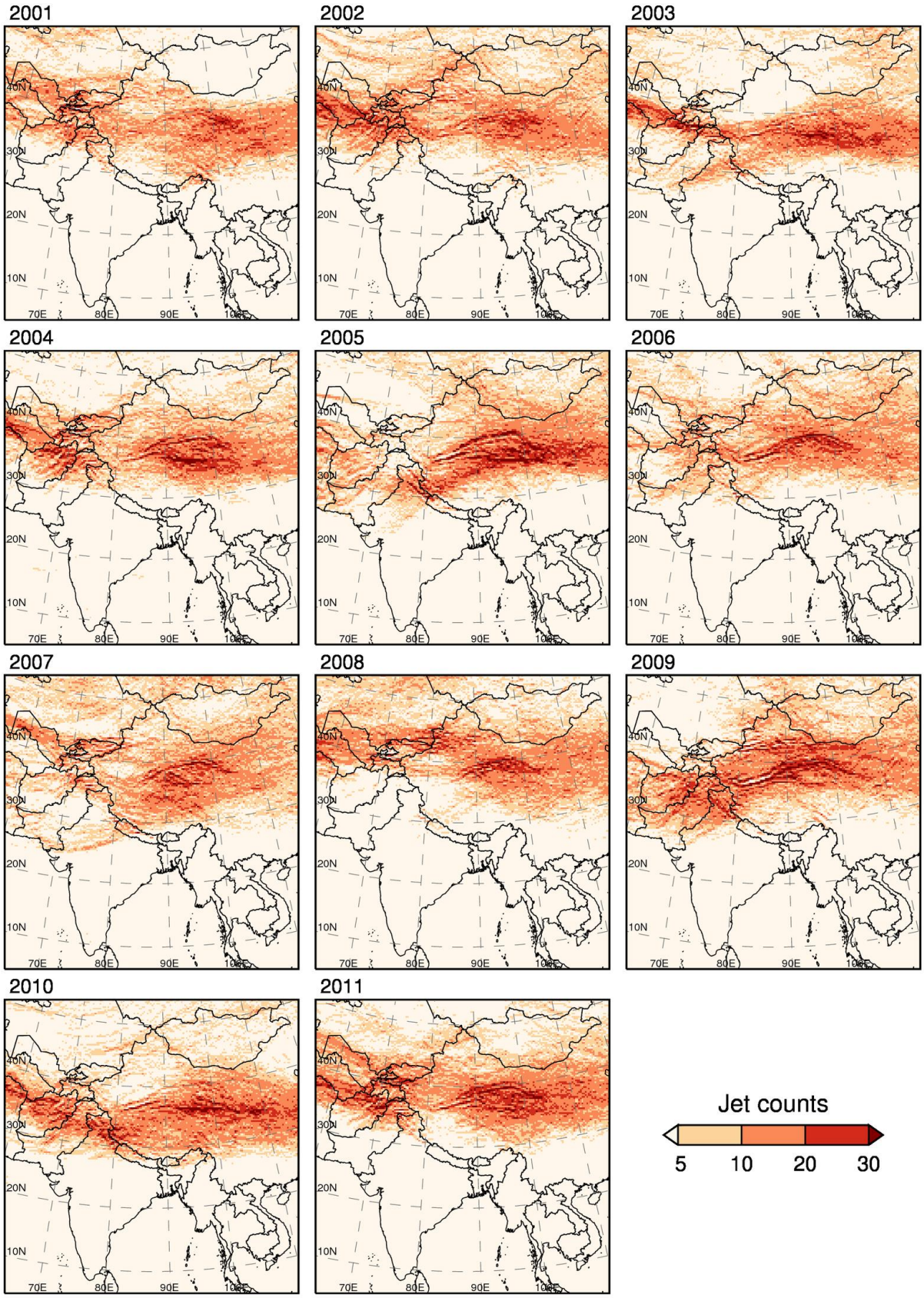

Figure S5: Westerly jet occurrences during the ISM onset period, 2001-2011, determined from HAR domain 1 data every three hours with the method of Schiemann et al. (2009). The lateral zone of the domain (ten grid points) is excluded from the analysis.

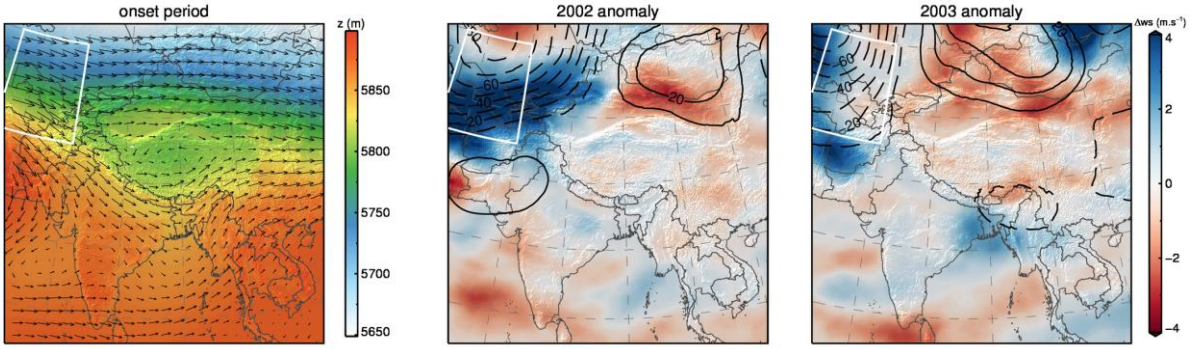

Figure S6: (Left) Mean wind vectors and geopotential height at 500 hPa in the ISM onset period, 2001-2011, in HAR domain 1. (Middle and right) Anomalies in wind speed (colour) and geopotential height (negative/positive shown as dashed/solid contours every 10 m) during the 2002 and 2003 ISM onset periods. The white fringe indicates the WEST region (see Fig. 1a). In 2002/2003, areas of stronger winds in the north-west of the domain (driven by geopotential height anomalies that intensify the north-south pressure gradient) indicate enhanced moisture advection toward the Tibetan Plateau cyclonic system, while the mostly below-average wind speeds over the plateau imply more time for local precipitation production (Kirshbaum and Durran, 2004; Fuhrer and Schär, 2005). The lateral zone of the domain (ten grid points) is excluded from the analysis

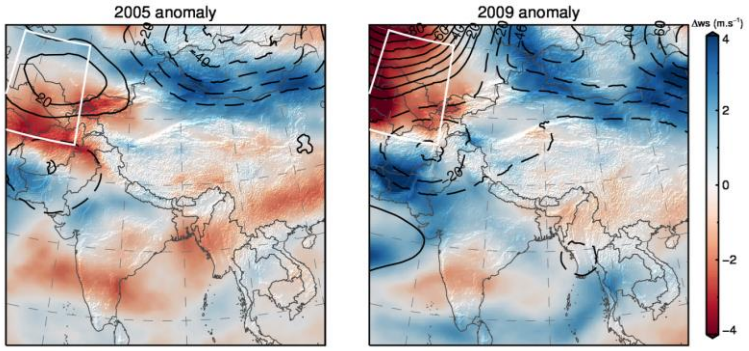

Figure S7: As Fig. S6 but for the ISM onset periods 2005 and 2009. Compared to Fig. S6, opposite geopotential height anomalies (i.e., a reduced north-south pressure gradient) and areas of reduced wind speeds upstream of the Tibetan Plateau are evident.

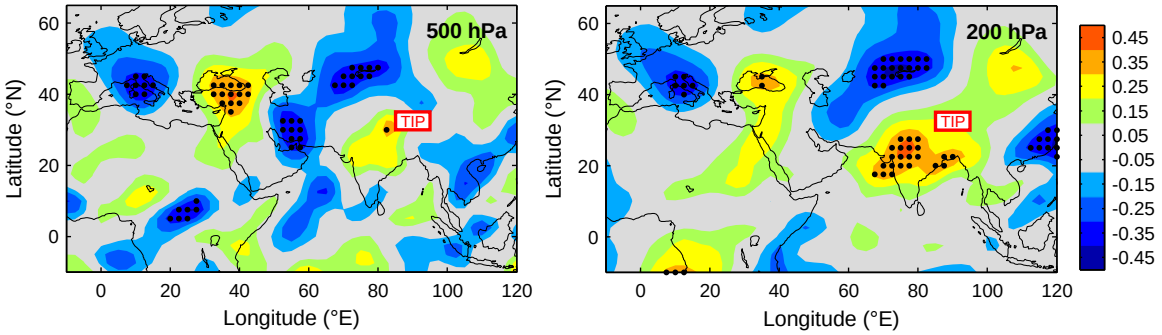

Figure S8: Correlation coefficient between area-averaged wind speed at 300 hPa over TIP and meridional winds at (left) 500 hPa and (right) 200 hPa in the ISM onset period, 1948-2011 (NCEP/NCAR reanalysis data). Dots locate grid points where correlations are significant ($p < 0.01$).

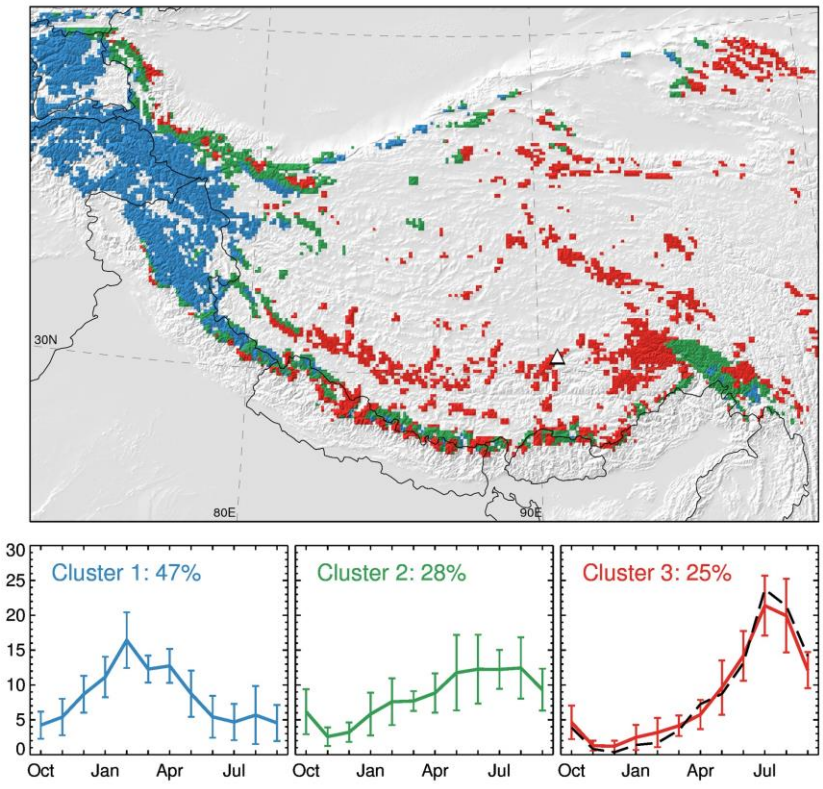

Figure S9: (Top) Distribution of the three accumulation regimes identified in the cluster analysis (Supplementary Methods) for all grid cells that contain glaciers, and (bottom) the mean annual cycles of precipitation for each regime, 2001-2011, as monthly percentage of the annual amount. Error bars are ± 1 σ of the grid cells per cluster. The black line in the annual cycle for Cluster 3 is Zhadang Glacier's grid cell, which shows that the glacier represents its cluster very well. The three percentages refer to the total glacier surface area in the domain, based on the Randolph inventory. In the map, Zhadang's location is indicated by the white triangle.

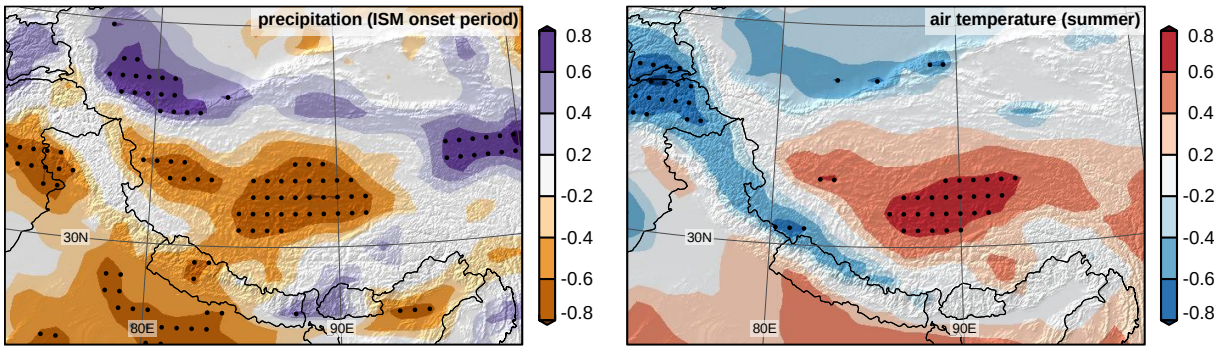

Figure S10: Correlation coefficient between wind speed at 300 hPa in the ISM onset period over the TIP region (Fig. 1a) and (left) precipitation in the same period and (right) mean 2-m air temperature in June/July/August in the High Asia domain, 2001-2011. Dots locate grid points where correlations are significant ($p < 0.05$). This figure is as Fig. 5 but uses ERA-Interim global reanalysis for all three variables, to show that the main correlation patterns are consistent with Fig. 5. Therefore, TIP wind speed linkages based on the higher-resolution HAR (Fig. 5) are (*i*) not an artificial result of HAR, and (*ii*) synoptically (large-scale) driven phenomena because they appear in the global data set (although HAR adds considerable regional detail, see Fig. 5). Note that ERA-Interim is generated independently from the NCEP/NCAR reanalysis (which is used as the global reference data set in this study) and the Global Final Analysis (which provides the boundary conditions for the HAR production).

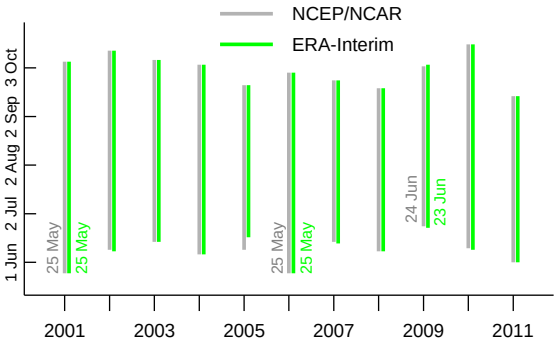

Figure S11: Annual duration of the ISM circulation, 2001-2011, determined from NCEP/NCAR and ERA-Interim reanalysis (see Supplementary Methods). Dates in the plot show earliest and latest onsets in the two data sets, which suggests the *ISM onset period* is robust. It only differs by one day, which has a negligible influence on the paper results relying on NCEP/NCAR data (Fig. 1b).

2 Supplementary Methods

Explicit atmospheric/mass-balance modelling

The usual way to model glacier mass-balance (MB) in high mountains from large-scale atmospheric data was to include statistical downscaling models, in particular to bypass the mesoscale (mountain-induced) atmospheric processes, see Mölg and Kaser (2011) for a detailed discussion. Only high-resolution atmospheric modelling (on the order of 1-10 km horizontal grid spacing) enables to represent glaciated elevations in atmospheric models explicitly, and therefore to use the output at such elevations without further statistical downscaling for MB modelling. This was first demonstrated by Mölg and Kaser (2011) through a tropical test study, and in the meantime has been applied to specific questions (Mölg et al., 2012b) and to other regions (Collier et al., 2013). The studies cited considered seasonal time slices, but here we extend the explicit approach to a full decade.

HAR-MB model combination and uncertainty quantification (error bars)

Meteorological conditions from the 10-km HAR domain at the grid cell containing Zhadang Glacier (Fig. S1) are input hourly to the MB model (Mölg et al., 2009a, 2012a). This grid cell is specified as "glacier surface" in the atmospheric model used for the HAR production. The grid cell altitude (5611 m) falls within the altitude range of the 657 grid cells in the 60-m resolution terrain model of Zhadang Glacier (5516-5983 m; Fig. 1, inset). Hence, no statistical downscaling is required to transfer the HAR variables to a reference point in the glaciated elevation zone. Cloud cover fraction is calculated from the total condensate mixing ratio (Mölg and Kaser, 2011).

Using the procedure described in detail in Mölg et al. (2012a), 29 parameters of the MB model are first varied within their physically meaningful range (Table S2) in 1000 simulations for the AWS1 site on Zhadang Glacier. Three of these parameter combinations are maintained for the distributed MB model runs. One reflects the best reproduction of the observed surface height change on the glacier (Fig. 2a), and the other two are the ones with largest positive and negative deviations from the measured daily surface height change, which are still within 10% root-mean-square difference relative to the measured amplitude. These two runs spread the uncertainty (error bars) around the "best run". See Mölg et al. (2012a), in particular their appendix, for a detailed description/illustration of the uncertainty procedure. The MB model has been confirmed in various climate zones (Mölg et al., 2009a/b, 2012a; Winkler et al., 2009; MacDonell et al., 2012).

Large-scale data and climate indices (incl. monsoon onset and active/break cycle)

The regions for the analysis of large-scale climate data (Fig. 1a) are delineated as follows: WEST (55-70° E, 35-50° N); ISM (65-105° E, 5-27.5° N; see Ding (2007)); GTI (60-70° E, 35-40° N; see Ding and Wang (2005)); and TIP (85-95° E, 30-35° N). The WEST region was chosen to cover the area upstream of the Tibetan Plateau, where mid-latitude cyclonic activity is the main cause of the springtime precipitation maximum (Aizen et al., 1997).

The duration of the Indian Summer Monsoon (ISM) circulation is obtained from the horizontal wind shear index (HWSI) as defined by Prasad and Hayashi (2007): area-averaged 850 hPa zonal wind in a southern region (40-80° E, 5-15° N) minus the one in a northern region (70-90° E, 20-30° N), see Fig. 1a. Active (break) ISM days are defined as days with HWSI > 1 sigma (wind in the northern region >1.5 sigma), which allows to identify the onset date of the ISM, see Mölg et al. (2012a) and their figure 4. After ISM onset, the succession of active and break phases characterizes the ISM's intra-seasonal variability (Prasad and Hayashi, 2007). The GTI is calculated as the area-averaged anomaly from the seasonal mean of the 200 hPa geopotential height (Ding and Wang, 2005).

TRMM precipitation (Huffman et al., 2007) was retrieved from <http://gdata1.sci.gsfc.nasa.gov/daac-bin/G3/gui.cgi?instance_id=TRMM_3B42_Daily>, NCEP/NCAR reanalysis (Kalnay et al., 1996) from <http://www.esrl.noaa.gov/psd/data/gridded/data.ncep.reanalysis.html>, and ERA-Interim (Dee et al., 2011) from <http://data-portal.ecmwf.int/data/d/interim_moda/levtype=pl/>.

The GTI index and diagnosis of westerly-monsoon interactions

The GTI describes a bridging mechanism between the upper-tropospheric mid-latitude circulation and the lower-tropospheric monsoon flow through surface heat low variability over Iran and Afghanistan (Saeed et al., 2011). In the positive phase of the GTI (i.e., positive seasonal anomaly of the 200 hPa geopotential height), moist flow from the Arabian Sea is able to penetrate further north. The role of the heat low as bridge in the monsoon-west wind interaction is reflected in our 2001-2011 data, since the GTI maintains a positive correlation with ISM precipitation (0.72 in the ISM onset period) but a negative one with WEST precipitation (–0.79 in May; $p < 0.05$ for both).

The studies of Bothe et al. (2011) and Saeed et al. (2011) demonstrated in detail that the interaction between the two systems can be diagnosed by geopotential height variability in the middle and upper troposphere. This implies that pressure anomalies and gradients are vital in the interaction, which also appears in our results and is discussed in connection with Figs. S6 and S7. In general, the pressure/geopotential height anomalies affect moisture transports from the monsoon zone, which contribute to climate variability in Asia (Bothe et al., 2011; Saeed et al., 2011).

Cluster analysis of glacier regimes

The cluster analysis of monthly precipitation (2001-2011), expressed as monthly percentage of the annual sum, serves to identify locations where a similar annual cycle in precipitation occurs (Kansakar et al., 2004). Here we use k-means clustering (e.g., Wilks, 2006) and obtain three basic regimes of accumulation on the glaciers of the High Asia domain (Fig. S9). The analysis is stable, since the attempt to add a fourth cluster results in the same three clusters as output (i.e., the fourth cluster is empty). The two expected classes are "winter accumulation" (Cluster 1) that prevails in the northwest of the mountain system (e.g., Karakoram, Pamir, Hindu Kush), and "summer accumulation" (Cluster 3) that dominates on the plateau. The analysis produces a further class (Cluster 2), which shows a less concentrated wet season and most precipitation between April and September. Cluster 2 is most obvious in the southeast of the mountain system and, otherwise, occurs in narrow zones along the southern and north-western fringes. Grid cells are included in the analysis if they contain glaciers, the boundaries of which are from the Randolph Glacier Inventory 2.0 (Arendt et al., 2012).

3 Supplementary Tables

Table S1: Squared correlation coefficient (i.e., explained variance) and significance level for different predictors of annual MB (Fig. 2d) in single or multiple linear regressions. Precipitation in the WEST region in May, precipitation in the ISM region in the ISM onset period, and 300 hPa wind speed in the TIP region in the ISM onset period; The "adjusted" r^2 is given in parentheses for multiple predictors, which – unlike the standard r^2 – accounts for the number of predictors in a model.

Independent variable	r^2	p
WEST	0.05	> 0.1
ISM	0.16	> 0.1
ISM + WEST	0.52 (0.40)	< 0.06
TIP wind speed	0.73	< 0.01
TIP wind speed + ISM + WEST	0.82 (0.75)	< 0.01

Table S2: Parameter ranges in the MB model, reproduced from Table A1 in Mölg et al. (2012a). Bold parameters indicate structural uncertainty, others parametric uncertainty. For the Monte Carlo simulation (N = 1000), values are assigned randomly from a uniform distribution, except for case 13 (normal distribution) since the authors provide uncertainty as one standard deviation (Gromke et al., 2011). See Mölg et al. (2012a) for references of the parameter ranges used. The only differences here are that (*i*) the parameters "initial snow depth altitudinal gradient" and "initial snow density" are redundant, since the model runs start without snow cover on 1 January 2001 (this initialisation has no effect on the model performance in Fig. 2), and (*ii*) two new parameters are allowed to vary (cases 28 and 29). $L\downarrow$ ($S\downarrow$) is incoming longwave (shortwave) radiation, α is surface albedo.

	Parameter(isation)	Value / Scheme	Note
1	vertical air temperature gradient (night/morning: >21-13 local time)	–0.0035 K m^{-1} ±10%	
2	vertical air temperature gradient (day: >13-21 local time)	–0.0095 K m^{-1} ±10%	
3	vertical precipitation gradient	+0.038 ± 0.026% m^{-1}	
4	upper threshold for precipitation phase (all liquid above)	6.5 ± 0.5 °C	
5	lower threshold for precipitation phase (all solid below)	1 ± 1 °C	
6	**parameterisation of $L\downarrow$**	two schemes	a
7	layer thickness for surface temperature scheme	0.5 m ± 10%	
8	**parameterisation of stable condition effect on turbulence**	two schemes	b
9	clear-sky diffuse radiation fraction	0.046 ± 20%	
10	cloud effect in radiation scheme	0.55 ± 10%	
11	roughness length ice (wind)	1.7 ± 1 mm	
12	roughness length ice (scalars)	1.7 ± 1 mm	
13	roughness length fresh snow	0.24 ± 0.05 mm	
14	roughness length aged snow (wind)	4 ± 2.5 mm	
15	roughness length aged snow (scalars)	4 ± 2.5 mm	
16	density of solid precipitation	250 ± 70 kg m^{-3}	c
17	superimposed ice constant	0.3 ± 20%	
18	fraction of $S\downarrow$ $(1 - \alpha)$ absorbed in surface layer (ice)	0.8 ± 10%	
19	fraction of $S\downarrow$ $(1 - \alpha)$ absorbed in surface layer (snow)	0.9 ± 10%	
20	extinction of penetrating shortwave radiation (ice)	2.5 m^{-1} ± 20%	
21	extinction of penetrating shortwave radiation (snow)	17.1 m^{-1} ± 20%	
22	fixed bottom temperature	268.6 ± 0.2 K	
23	ice albedo	0.3 ± 0.1	d
24	firn albedo	0.53 ± 0.1	c
25	fresh snow albedo	0.85 ± 0.03	
26	albedo time scale	6 ± 3 days	
27	albedo depth scale	8 ± 6 cm	
28	snowfall event threshold	0.7 ± 0.3 cm	e
29	precipitation scaling factor	0.65 ± 0.15	f

a: Mölg et al. (2009b) or Klok and Oerlemans (2002); **b**: equation 11 or 12 in Braithwaite (1995); **c**: range slightly wider than in Mölg et al. (2012a); **d**: Accelerated retreat of alpine glaciers may lead to an increased transport of dust (from the increasingly exposed side moraines) to the ice surface, which decreases ice albedo on the decade-scale (Oerlemans et al., 2009). We have no evidence that this matters at Zhadang. Also, the glacier's retreat rate has not changed substantially since 2001 compared to previous decades (Bolch et al., 2010). **e**: If the sum of uninterrupted snowfall exceeds this threshold, the snowfall counts as *event* in the albedo parameterisation (Oerlemans and Knap,

1998). Previous modelling showed that the parameterization works best if this value is between ~0.5 and ~1 cm (Mölg et al., 2009a, 2012a); **f**: Atmospheric model precipitation is multiplied by this factor to account for atmospheric model errors and wind drift effects on snowfall. Mölg et al. (2012a) obtained 0.56 for 2009-2011, but here we consider a range to allow a possibly more representative value for the longer interval 2001-2011.

Table S3: Mass balance (kg m^{-2}) averaged over stake locations (Fig. 1a, inset) for the available three seasonal measurement intervals. Model uncertainty as defined in Supplementary Methods, measurement uncertainty is typically 200-300 kg m^{-2} per year (e.g., Braithwaite and Olesen, 1989), thus we assign 250 kg m^{-2} per year, scaled by the number of days in the interval.

	3 Sep./09-17 May/10	2 Jun.-13 Jul./09	17 May-28 Sep./10
measurement	–132 ± 176	–1493 ± 29	–2554 ± 92
HAR-MB model	–258 ± 30	–1397 ± 102	–2404 ± 97

Table S4: Annual MB of four glaciers on the Tibetan Plateau. Measurements refer to the "mass-balance year" (1 October of previous year to 30 September) and are from Yao et al. (2012), while Zhadang data are given for the calendar year and the mass-balance year (parentheses). The highest and lowest MBs in the period with overlapping data (2008-2010) are highlighted in green and red, respectively. See further in Supplementary Discussion.

	Gurenhekou *measurement* (Yao et al., 2012)	Xiaodongkemadi *measurement* (Yao et al., 2012)	Zhadang *modelled/constrained by measurements* (this study)	Zhongxi *measurement* (Yao et al., 2012)
1989		525		
1990		45		
1991		–180		
1992		375		
1993		210		
1994		–510		
1995		–570		
1996		–495		
1997		345		
1998		–690		
1999		–315		
2000		–90		
2001		–195	21 ± 251	
2002		–583	45 ± 169 (–1 ± 174)	
2003		4	–63 ± 121 (–22 ± 119)	
2004		–153	208 ± 99 (146 ± 97)	
2005		–177	–1902 ± 53 (–1817 ± 59)	
2006	–319	–917	–2727 ± 51 (–2779 ± 54)	
2007	–196	–591	–1643 ± 210 (–1630 ± 227)	
2008	497	–80	–109 ± 423 (–178 ± 417)	264
2009	–839	–91	–1941 ± 154 (–1939 ± 152)	–1045
2010	–703	–1066	–1481 ± 63 (–1480 ± 68)	–789
2011			–213 ± 173 (–160 ± 178)	

4 Supplementary Discussion

Performance of the combined HAR-MB modelling system

The performance for surface height change (Fig. 2a) and glacier surface temperature (Fig. 2b) at the AWS1 location resembles the performance when the MB model is driven largely by measurements from AWS1: Mölg et al. (2012a) used *measured* hourly air temperature, relative humidity, wind speed, air pressure, and wintertime precipitation, and in addition started the MB model run only at the time when measurements begun, and obtained a root-mean-square difference of 7.3 cm for surface height change and 1.7 K for daily glacier surface temperature, compared to 15.6 cm (only 5% of the measured amplitude) and 2.1 K with all drivers from the atmospheric model-based HAR data (Fig. 2a/b). The spatially distributed evaluation at stake locations (Fig. 2c) yields a further satisfying result, since the point scatter in Fig. 2c is not larger, or even smaller, than the one from distributed and physically-based MB models entirely driven by AWS measurements (e.g., Hock and Holmgren, 2005). The high correlation (0.97) indicates that the model reproduces the seasonal MB characteristics well, and the area-averaged mass flux over the stake locations is consistent between model and measurements for the single seasons (Table S3). Therefore, since the combined HAR-MB modelling system is confirmed by all available measurements, it very likely captures the principal processes of the glacier-atmosphere interactions.

Jet position and mass-balance in the year 2006

In 2006 a large negative MB (Fig. 2d) coincides with a northern jet position (Fig. S5), although the latter seems to be favourable for above-average MB in the analysis of the other ten years. However, 2006 is the only year when both WEST and ISM circulation intensities are below average (Fig. 1b), and in such a case the favourable jet position seems unable to help prevent a negative MB. A rather high wind speed over the plateau in 2006 in the NCEP/NCAR reanalysis (Fig. 1c), moreover, indicates that the meridional distance of the jet was not the main control of the tropospheric flow strength in this single year.

Tibetan Plateau flow strength and the circumglobal wave train

The vorticity gradients that accompany the high-level westerly jet can form a wave train, which is meridionally trapped and therefore propagates far downstream before the energy is dissipated (Branstator, 2002). The associated Rossby waves span a circumglobal pattern (Branstator, 2002) of which the European-Asian wave train is a regional segment (Ding and Wang, 2005). The waves are diagnosed in the meridional wind variability in the upper troposphere at 200 or 300 hPa (Bothe et al., 2011), see Fig. 4 in the main paper. Recent studies also found that the high-level westerly jet (Sato, 2009) and the wave train (Bothe et al., 2011, 2012) have a major impact on Tibetan Plateau drought and wetness. This supports Fig. 4, showing that wind speed over the plateau and thus glacier MB maintain links with the mid-latitude westerly wave dynamics (for example, cf. Fig. 8 in Bothe et al. (2011) for zero lead/lag). Also, wet summers over the Tibetan Plateau show a more zonally oriented teleconnection route (Bothe et al., 2011), which fits to the result that rather weak onsets of the precipitation season like 2005-2007 and 2009 show a relatively weak zonal component in the 300 hPa wind speed over the plateau (i.e., difference between the two curves in Fig. 1c is relatively large for these years).

Direct mass-balance measurements

For the discussion of regional representativity, we tried to consider all available MB measurements at annual resolution on glaciers, which are situated in the large area of statistically significant correlations of TIP wind speed with *both* precipitation and summer air temperature (Fig. 5). The available observations (Gurenhekou, Zhangxi, and Xiaodongkemadi Glacier) are based on stake measurements with the direct glaciological method (Yao et al., 2012). Table S4 compiles the MBs of

these glaciers and our MB results for Zhadang. The period with overlapping data is short, but all glaciers experienced the highest MB in 2008, and three of the four glaciers had the lowest MB in 2009.

The annual MB for Zhadang in Fig. 2d and Fig. 5 is from 1 January to 31 December, but the "mass-balance year" can also be defined from 1 October to 30 September of the subsequent year. The latter is the case for the three measured records in Fig. 5 and Table S4. However, since meteorological conditions on the southern and central Tibetan Plateau are characterized by little winter precipitation (e.g., Fig. S1), the MB over the calendar year is very close to the one over a mass-balance year. This is evident in the Zhadang data: for 2001/2002-2011 the root-mean-square difference in annual MB for the two different time windows (N = 10 pairs) is only 50 kg m^{-2} (cf. Table S4), which is 5.6% of the mean MB 2001-2011 (–891 kg m^{-2} year^{-1}). We preferred to work with the calendar year in this study, which allowed us to use eleven instead of ten annual MBs of Zhadang.

Absolute differences in mean mass-balances (all units in kg m^{-2} year^{-1})

The mean modelled glacier-wide MB of Zhadang over 2001-2011 is –891 ± 105, which is lower than the mean MBs from the direct glaciological method in Table S4: –312, –236, and –523 for Gurenhekou, Xiaodongkemadi, and Zhongxi, respectively. Mean MBs derived from satellite data are also mostly less negative than Zhadang's modelled MB. For example, Gardner et al. (2013) give –270 ± 160 for South and East Tibet (2003-2008), and Gardelle et al. (2013) obtain between –220 ± 130 and –450 ± 140 (1999-2011) for the mountains that margin the Tibetan Plateau in the south. Gardner et al. (2013), however, report a more negative value for East Himalaya than Gardelle et al. (2013), –800 ± 220. And Bolch et al. (2011), combining aerial and satellite images in the Nepal Himalaya, obtained a mean for ten glaciers of –790 ± 520 (and MBs for single glaciers as low as –1000 to –1500) over 2002-2007. Zhadang's MB is thus representing the lower end of these regional estimates. While the different averaging intervals and spatial references (single glacier vs. regional mean) explain a part of the MB differences, there are a number of other possible sources.

(*i*) The general lack of field data from the accumulation zone, which introduces uncertainty to, first, deriving "measured" glacier-wide MBs (e.g., Table S4) from data concentrated in the ablation zone, and second, to modelling as well since MB models can rarely be evaluated for the accumulation zone as extensively as for the ablation zone (which is also the case here). (*ii*) The delineation of glacier outlines in satellite-based studies. For instance, Gardelle et al. (2013) obtain –700 ± 520 and Bolch et al. (2011) give –1450 ± 520 for the same glacier (Lhotse Shar/Imja). And finally, (*iii*) peculiarities of the local environment of the glacier (e.g., area-altitude distribution, avalanches and snow drift, debris) modify the influence of larger-scale climate drivers common to a region. Yet the different MBs and studies outlined above leave no doubt that the southern and eastern Tibetan Plateau, as well as the mountains in southern and south-western High Asia, are presently characterized by widespread glacier mass loss. In our study, the absolute differences in mean MB are of limited importance, since our findings are based on the inter-annual MB variability.

5 Supplementary Notes

This work was supported by the Alexander von Humboldt Foundation and the German National Academy of Sciences (T. Mölg), by the German Research Foundation (DFG) Priority Programme 1372, "Tibetan Plateau: Formation – Climate – Ecosystems" within the DynRG-TiP ("Dynamic Response of Glaciers on the Tibetan Plateau to Climate Change") project under the codes SCHE 750/4-1, SCHE 750/4-2, SCHE 750/4-3, and by the German Federal Ministry of Education and Research (BMBF) Programme "Central Asia – Monsoon Dynamics and Geo-Ecosystems" (CAME) within the WET project "Variability and Trends in Water Balance Components of Benchmark Drainage Basins on the Tibetan Plateau" under the code 03G0804A. We thank M. Buchroithner, J. Curio, N. Holzer, E. Huintjes, O. Käsmacher, J. Kropáček, T. Pieczonka, J. Richters, T. Sauter, C. Schneider, B. Schröter, M. Spieß, W. Wang, and the local Tibetan people for their participation in field work. We also thank T. Yao, S. Kang, W. Yang, G. Zhang, and the staff of the Nam Co monitoring station from the Institute of Tibetan Plateau Research, Chinese Academy of Sciences, for leading the glaciological measurements on Zhadang and for providing ablation stake data. Three anonymous reviewers provided excellent comments on earlier versions of the paper.

References in Supplementary Material

Aizen V.B., Aizen E.M., Melack J.M., Dozier J. (1997): Climatic and hydrologic changes in the Tien Shan, Central Asia. *Journal of Climate*, **10**: 1393–1404.

Arendt A., and 77 others (2012): *Randolph Glacier Inventory [v2.0]: a Dataset of Global Glacier Outlines, Global Land Ice Measurements from Space*. Digital media, available at http://www.glims.org/RGI/.

Bolch T., Yao T., Kang S., Buchroithner M.F., Scherer D., Maussion F., Huintjes E., Schneider C. (2010): A glacier inventory for the western Nyainqentanglha Range and the Nam Co Basin, Tibet, and glacier changes 1976–2009. *The Cryosphere*, **4**: 419–433.

Bolch T., Pieczonka T., Benn D.I. (2011): Multi-decadal mass loss of glaciers in the Everest area (Nepal Himalaya) derived from stereo imagery. *The Cryosphere*, **5**: 349–358.

Bothe O., Fraedrich K., Zhu X. (2011): Large-scale circulations and Tibetan Plateau summer drought and wetness in a high-resolution climate model. *International Journal of Climatology*, **31**: 832–846.

Bothe O., Fraedrich K., Zhu X. (2012): Tibetan Plateau summer precipitation: covariability with circulation indices. *Theoretical and Applied Climatology*, **108**: 293–300.

Braithwaite R.J., Olesen O.B. (1989): Detection of climate signal by inter-stake correlations of annual ablation data Qamanârssûp Sermia, West Greenland. *Journal of Glaciology*, **35**: 253–259.

Braithwaite R.J. (1995): Aerodynamic stability and turbulent sensible-heat flux over a melting ice surface, the Greenland ice sheet. *Journal of Glaciology*, **41**: 562–571.

Branstator G. (2002): Circumglobal teleconnections, the jet stream waveguide, and the North Atlantic Oscillation. *Journal of Climate*, **15**: 1893–1910.

Collier E., Mölg T., Maussion F., Scherer D., Mayer C., Bush A.B.G. (2013): High-resolution interactive modelling of the mountain glacier-atmosphere interface: An application over the Karakoram. *The Cryosphere*, **7**: 779–795.

Ding Q., Wang B. (2005): Circumglobal teleconnection in the northern hemisphere summer. *Journal of Climate*, **18**: 3483–3505.

Ding Y. (2007): The variability of the Asian Summer Monsoon. *Journal of the Meteorological Society of Japan*, **85B**: 21–54.

Dee D.P., and 35 others (2011): The ERA-Interim reanalysis: configuration and performance of the data assimilation system. *Quarterly Journal of the Royal Meteorological Society*, **137**: 553–597.

Fuhrer O., Schär C. (2005): Embedded cellular convection in moist flow past topography. *Journal of the Atmospheric Sciences*, **62**: 2810–2828.

Gardelle J., Berthier E., Arnaud Y., Kääb A. (2013): Region-wide glacier mass balances over the Pamir-Karakoram-Himalaya during 1999–2011. *The Cryosphere*, **7**: 1263–1286.

Gardner A.S., and 15 others (2013): A reconciled estimate of glacier contributions to sea level rise: 2003 to 2009. *Science*, **340**: 852–857.

Gromke C., Manes C., Walter B., Lehning M., Guala M. (2011): Aerodynamic roughness length of fresh snow. *Boundary-Layer Meteorology*, **141**: 21–34.

Hock R., Holmgren B. (2005): A distributed surface energy-balance model for complex topography and its application to Storglaciären, Sweden. *Journal of Glaciology*, **51**: 25–36.

Huffman G.J., Adler R.F., Bolvin D.T., Gu G., Nelkin E.J., Bowman K.P., Hong Y., Stocker E.F., Wolff D.B. (2007): The TRMM Multi-satellite Precipitation Analysis: Quasi-Global, Multi-Year, Combined-Sensor Precipitation Estimates at Fine Scale. *Journal of Hydrometeorology*, **8**: 38–55.

Kalnay E., and 21 others (1996): The NCEP/NCAR 40-year reanalysis project. *Bulletin of the American Meteorological Society*, **77**: 437–471.

Kansakar S.R., Hannah D.M., Gerrard J., Rees G. (2004): Spatial pattern in the precipitation regime of Nepal. *International Journal of Climatology*, **24**: 1645–1659.

Kirshbaum D.J., Durran D.R. (2004): Factors governing cellular convection in orographic precipitation. *Journal of the Atmospheric Sciences*, **61**: 682–698.

Klok E.J., Oerlemans J. (2002): Model study of the spatial distribution of the energy and mass balance of Morteratschgletscher, Switzerland. *Journal of Glaciology*, **48**: 505–518.

MacDonell S.A., Fitzsimons S.J., Mölg T. (2012): Seasonal sediment fluxes forcing supraglacial melting on the Wright Lower Glacier, McMurdo Dry Valleys, Antarctica. *Hydrological Processes*, doi:10.1002/hyp.9444 (early view).

Mölg T., Cullen N.J., Hardy D.R., Winkler M., Kaser G. (2009a): Quantifying climate change in the tropical midtroposphere over East Africa from glacier shrinkage on Kilimanjaro. *Journal of Climate*, **22**: 4162–4181.

Mölg T., Cullen N.J., Kaser G. (2009b): Solar radiation, cloudiness and longwave radiation over low-latitude glaciers: Implications for mass-balance modelling. *Journal of Glaciology*, **55**: 292–302.

Mölg T., Kaser G. (2011): A new approach to resolving climate-cryosphere relations: Downscaling climate dynamics to glacier-scale mass and energy balance without statistical scale linking. *Journal of Geophysical Research*, **116**: D16101.

Mölg T., Maussion F., Yang W., Scherer D. (2012a): The footprint of Asian monsoon dynamics in the mass and energy balance of a Tibetan glacier. *The Cryosphere*, **6**: 1445–1461.

Mölg T., Großhauser M., Hemp A., Hofer M., Marzeion B. (2012b): Limited forcing of glacier loss through land-cover change on Kilimanjaro. *Nature Climate Change*, **2**: 254–258.

Oerlemans J., Knap W.H. (1998): A 1 year record of global radiation and albedo in the ablation zone of Morteratschgletscher, Switzerland. *Journal of Glaciology*, **44**: 231–238.

Oerlemans J., Giesen R.H., van den Broeke M.R. (2009): Retreating alpine glaciers: increased melt rates due to accumulation of dust (Vadret da Morteratsch, Switzerland). *Journal of Glaciology*, **55**: 729–736.

Prasad V.S., Hayashi T. (2007): Active, weak and break spells in the Indian summer monsoon. *Meteorology and Atmospheric Physics*, **95**: 53–61.

Saeed S., Müller W.A., Hagemann S., Jacob D. (2011): Circumglobal wave train and the summer monsoon over northwestern India and Pakistan: the explicit role of the surface heat low. *Climate Dynamics*, **37**: 1045–1060.

Sato T. (2009): Influences of subtropical jet and Tibetan Plateau on precipitation pattern in Asia: Insights from regional climate modeling. *Quaternary International*, **194**: 148–158.

Schiemann R., Lüthi D., Schär C. (2009): Seasonality and interannual variability of the westerly jet in the Tibetan Plateau region. *Journal of Climate*, **22**: 2940–2957.

Wilks D.S. (2006): *Statistical methods in the atmospheric sciences*. Academic Press, 2nd edition.

Winkler M., Juen I., Mölg T., Kaser G. (2009): Measured and modelled sublimation on the tropical Glaciar Artesonraju, Perú. *The Cryosphere*, **3**: 21–30.

Yao T., and 14 others (2012): Different glacier status with atmospheric circulations in Tibetan Plateau and surroundings. *Nature Climate Change*, **2**: 663–667.